Electronic Supplementary Information (ESI)

One-Step Electrodeposited MoS$_2$@Ni-mesh Electrode for Flexible and Transparent Asymmetric Solid-State Supercapacitors

Soram Bobby Singh[a], Dai Jiu Yi[a], Thangjam Ibomcha Singh[a], Nam Hoon Kim[a],

Joong Hee Lee[a, b],*

[a] Department of Nano Convergence Engineering, Jeonbuk National University, Jeonju, Jeonbuk, 54896, Republic

of Korea

[b]Carbon Composite Research Centre, Department of Polymer-Nano Science and Technology, Jeonbuk National

University, Jeonju, Jeonbuk 54896, Republic of Korea.

*Corresponding author: e-Mail: jhl@jbnu.ac.kr (Joong Hee Lee)

1. Electrochemical characterization

Electrochemical properties of the MoS$_2$@Ni-mesh and MnO$_2$@Ni-mesh network electrode were measured at room temperature in a three-electrode configuration using MoS$_2$@Ni-mesh and MnO$_2$@Ni-mesh as the working electrode, Ag/AgCl as the reference electrode, and a Pt plate as the counter electrode respectively in 1 M Na$_2$SO$_4$ electrolyte solution. In the case of the FT-ASSc device, two-electrode configuration mode was used to measure the electrochemical performance. All these electrochemical measurements were performed using a CH660E electrochemical workstation (CH Instruments, Inc., USA).

The areal capacitance (mF/cm^2) of the single electrode was also derived from the CV scan using the following equation:

$$C/A = \frac{1}{vA\Delta V}\oint I(V)dV$$

(1)

where A was the effective area of the single electrode, v (V/s) was the potential scan rate, and ΔV (V) was the window.

The C/A (in mF/cm^2) was also calculated from the galvanostatic charge/discharge (GCD) curves using Equation (2)

$$C/A = \frac{I}{A \times (dV/dt)}$$

(2)

where I is the discharge current (A), A is the total area of the electrodes (cm^2), and dV/dt is the slope of the galvanostatic discharge curve.

In the case of the two-electrode configuration system, the areal capacitance of the device was calculated based on the area of the device as according to the following Equation (3)

$$C_{device}^{areal} = \frac{1}{v A_{device} \Delta V} \oint I(V) dV \qquad (3)$$

$$C_{device}^{areal} = \frac{I}{A_{device} \times (dV/dt)} \qquad (4)$$

where C_{device}^{areal} (in mF/cm²) refer to the areal capacitance of the device and A_{device} is the total area (cm²) of the device electrodes, v (V/s) was the potential scan rate, and ΔV (V) was the operating window of the device, I is the discharge current (A), and dV/dt is the slope of the GCD curve , respectively.

The volumetric capacitance (C/V in mF/cm³) was also calculated from the galvanostatic charge/discharge (GCD) curves using Equation (5)

$$C/V = \frac{I}{V \times (dV/dt)} \qquad (5)$$

here I is the discharge current (A), V is the total volume of the device, and dV/dt is the slope of the galvanostatic discharge curve.

Energy densities and power densities were calculated using Equation (6) as follows

$$E = \frac{C \times (\Delta V)^2}{2 \times 3600} \qquad (6a)$$

$$P = \frac{E \times 3600}{\Delta t} \qquad (6b)$$

Where E is the energy density (Wh/cm²), C is the areal capacitance (F/cm²), ΔV is the discharge voltage range (V) and Δt is the discharge time (s)

2. Characterization

Surface morphologies of the electrode samples were studied using FE-SEM, Carl Zeiss, SUPRA 40 VP, Germany, at the Center for University-wide Research Facilities (CURF), Jeonbuk National University, Korea. The internal structure, elemental composition, and spatial distribution of constituent elements were investigated using a high-resolution transmission electron microscope (HRTEM), a scanning transmission electron microscope (STEM) (JEM-2200 FS; JEOL Ltd., Japan, 200 kV), and energy-dispersive X-ray spectroscopy (EDX). The chemical compositions and elemental states of MoS_2@Ni-mesh and MnO_2@Ni-mesh network electrode were studied using an X-ray photoelectron spectroscopy (XPS) (Theta Probe AR-XPS System, Thermo Fisher Scientific, UK) at the KBSI center, JBNU campus. Transparencies of electrode samples and devices were analyzed using Jasco-ARSN-733 UV-Vis-NIR spectroscopy. Using a four-point-probe surface resistivity meter (MSTEC) coupled with a Keithley-2182A nano voltmeter having a Keithley-6221 DC/AC current source the sheet resistance of the electrode samples were measured. Mechanical flexible properties were tested with a Radius Bending Tester-JIRBT-610 coupled with a Keithley-6221 DC/AC current source. All these electrochemical measurements were performed using a CH660E electrochemical workstation (CH Instruments, Inc., USA). Atomic force microscope (AFM; XE-100, Park System Co., Korea).
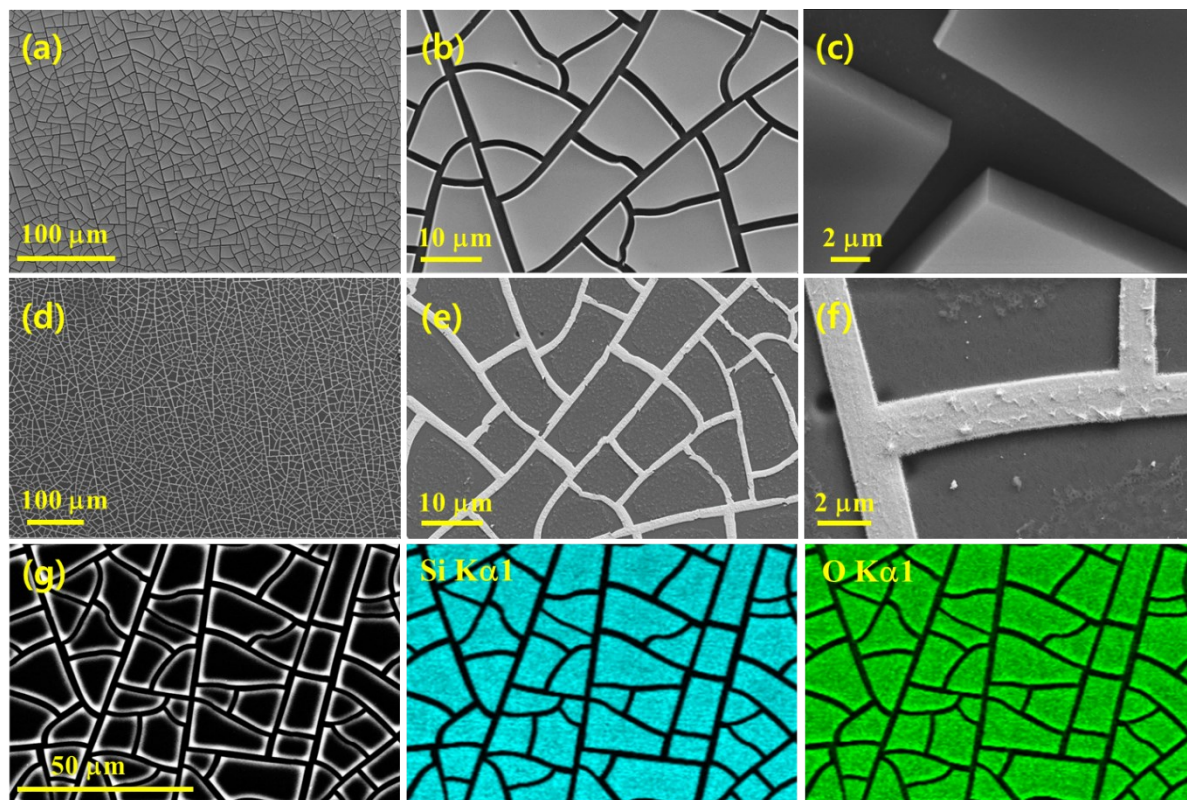
Supplementary Figures

Fig. S1 FE-SEM images : (a-c) cracked silica templated film. (d-f) Ni-mesh network at different magnifications after etching out silica template film. (g) EDS mapping image of Si-cracked templated film on PEN substrate.
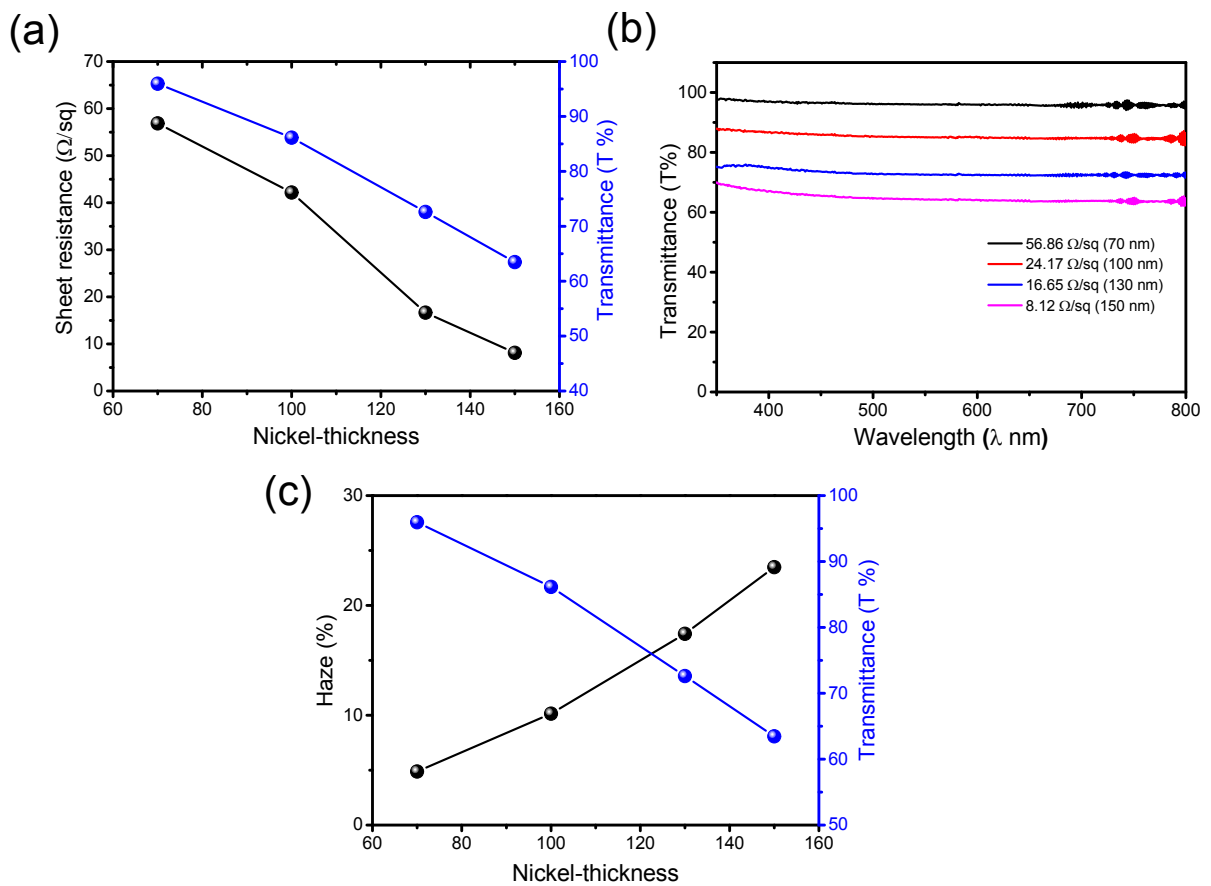
Fig. S2 (a) Sheet resistance and transmittance (at 550 nm) of Ni-mesh network as a function of the thickness of the Ni-mesh deposited. (b) UV-visible transmittance spectra of the Ni-mesh network on PEN substrate with various sheet resistances at different Ni-mesh thickness. (c) haze value (%) and transmittance of Ni-mesh network electrode (at 550 nm) as a function of Ni-thickness.
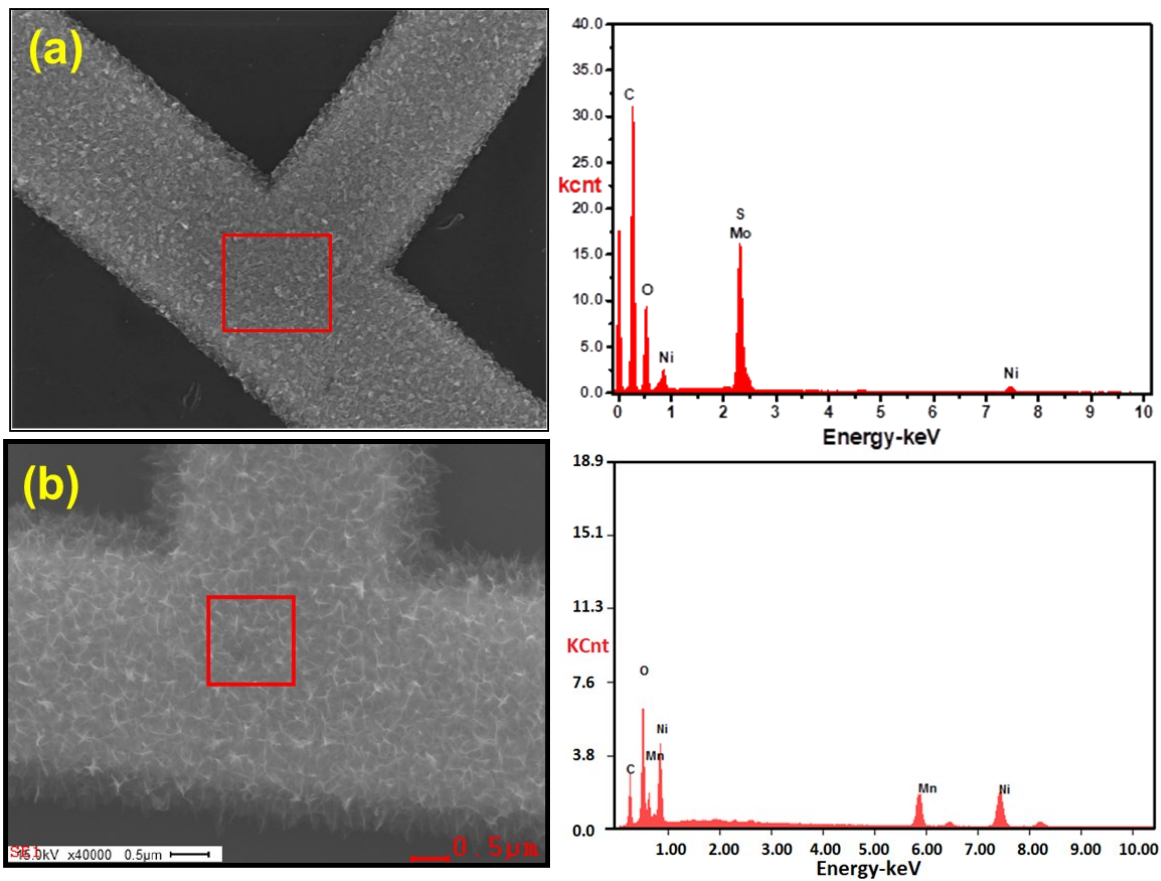
Fig. S3 EDAX spectra: (a) MoS_2@Ni-mesh network electrode. (b) MnO_2@Ni-mesh network electrode.
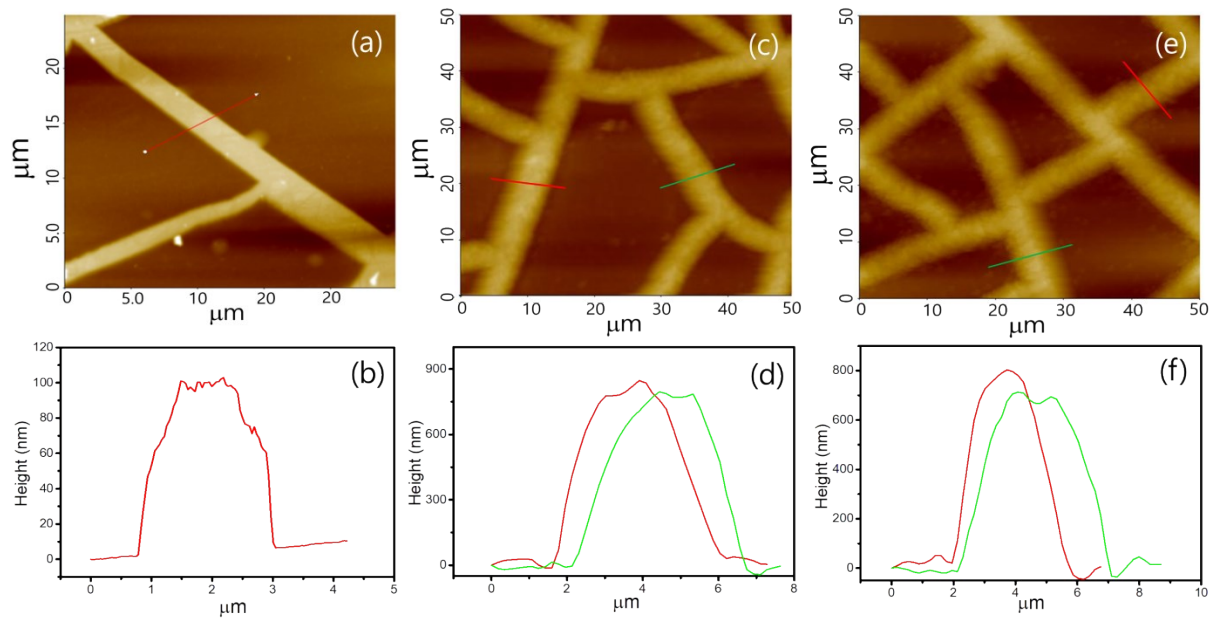
Fig. S4 2D-AFM and line profile analysis images: (a, b) pristine Ni-mesh, (c, d) MoS$_2$@Ni-mesh, (e, f) MnO$_2$@Ni-mesh on PEN substrate.
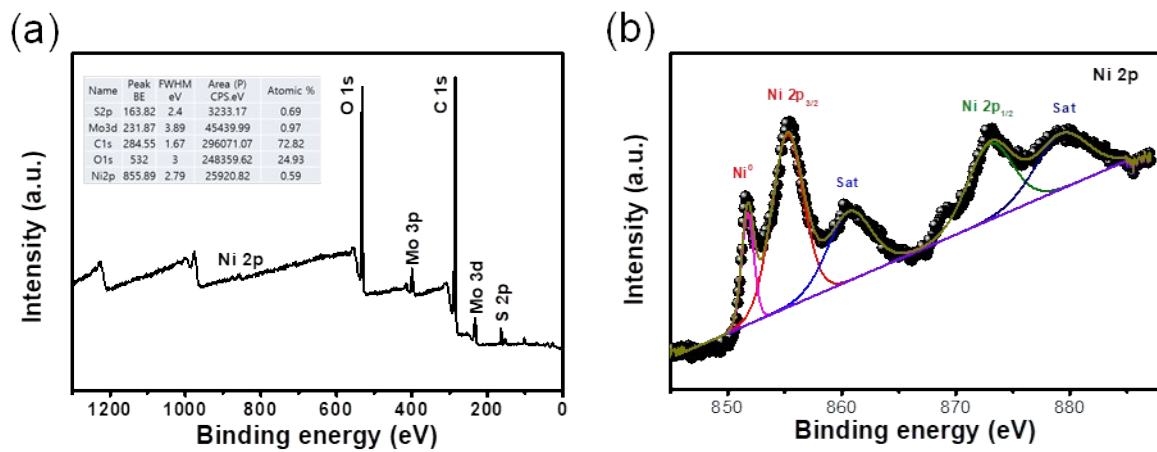
Fig. S5 (a) The full XPS survey spectrum of the MoS$_2$ nanosheet@Ni-mesh electrode. (b) High -

resolution fitted XPS spectra of Ni 2p of the MnO$_2$ nanosheet@Ni-mesh electrode.
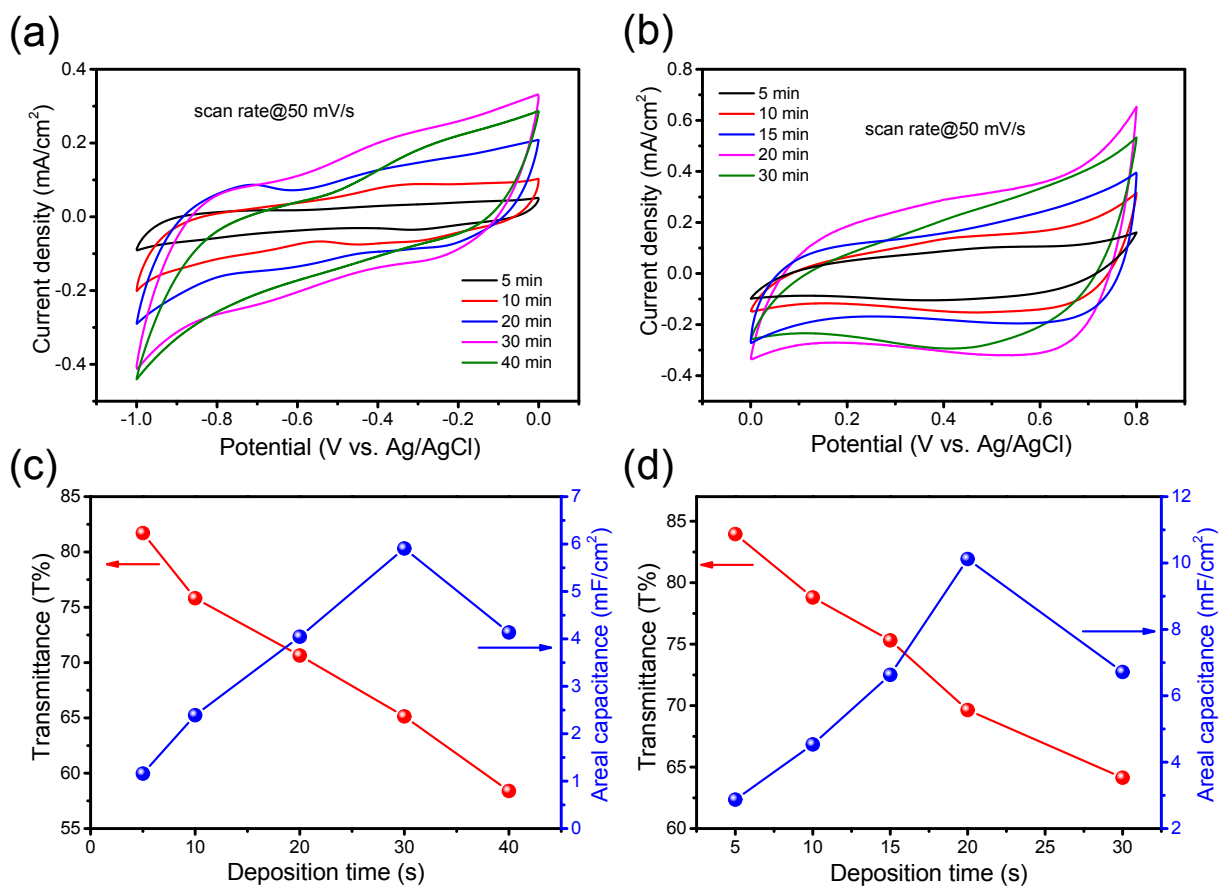
Fig. S6 (a) Electrochemical measurements of the MoS2@Ni-mesh and MnO$_2$@Ni-mesh network electrodes in a three-electrode configuration in 1 M Na$_2$SO$_4$ electrolyte. Cyclic voltammograms (CVs) of the electrodes with different electrodeposition times at a scan rate of 50 mV/s for (a) MoS$_2$@Ni-mesh and (b) MnO$_2$@Ni-mesh network electrode. (c, d) Optical transmittance and areal capacitance as a function of electrodeposition time (areal capacitance derived from Fig S4a, b) for MoS$_2$@Ni-mesh (c) and MnO$_2$@Ni-mesh (d) network electrodes.

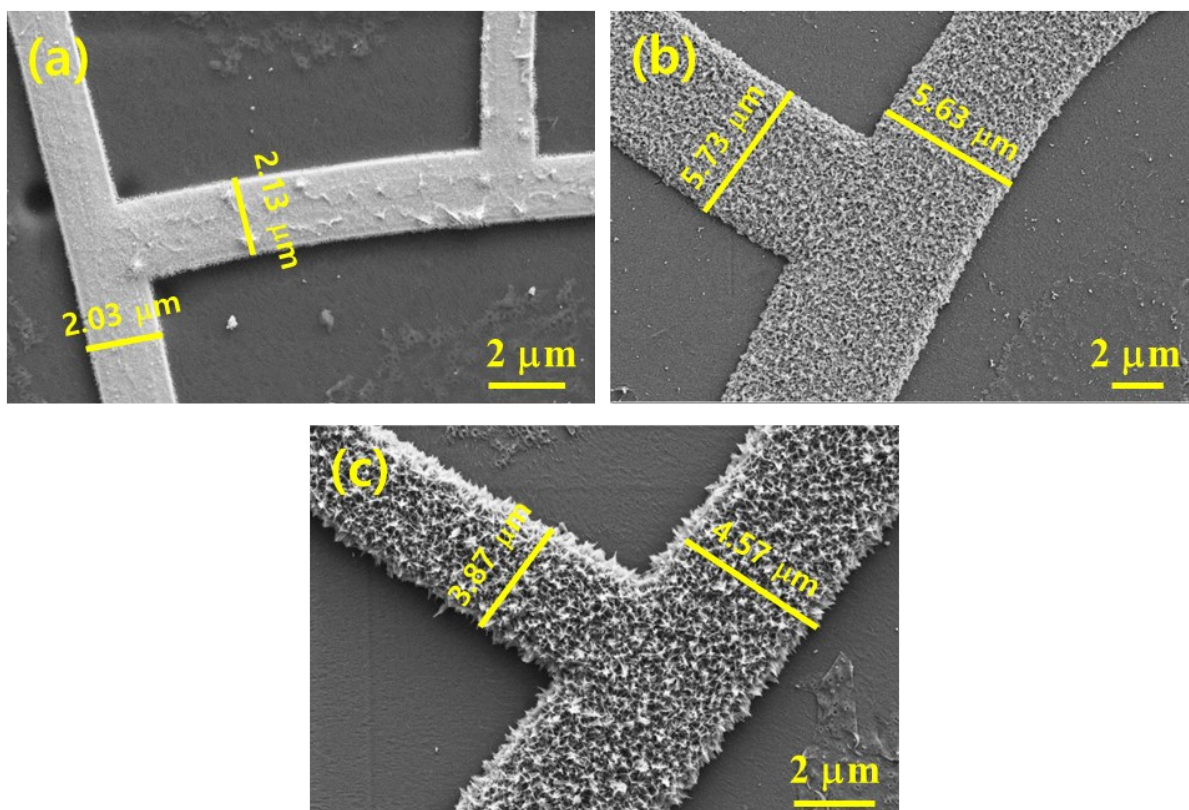**Fig. S7** FE-SEM photographs of: (a) Ni-mesh network electrode on PEN substrate (b) MoS$_2$@Ni-mesh network electrode on PEN substrate for 20 min electrodeposition time. (c) MnO$_2$@Ni-mesh network electrode on PEN substrate for 15 min electrodeposition time. Indicating a large increase in the width and thickness of the mesh network after electrodeposition of the respective MoS$_2$ and MnO$_2$ materials.
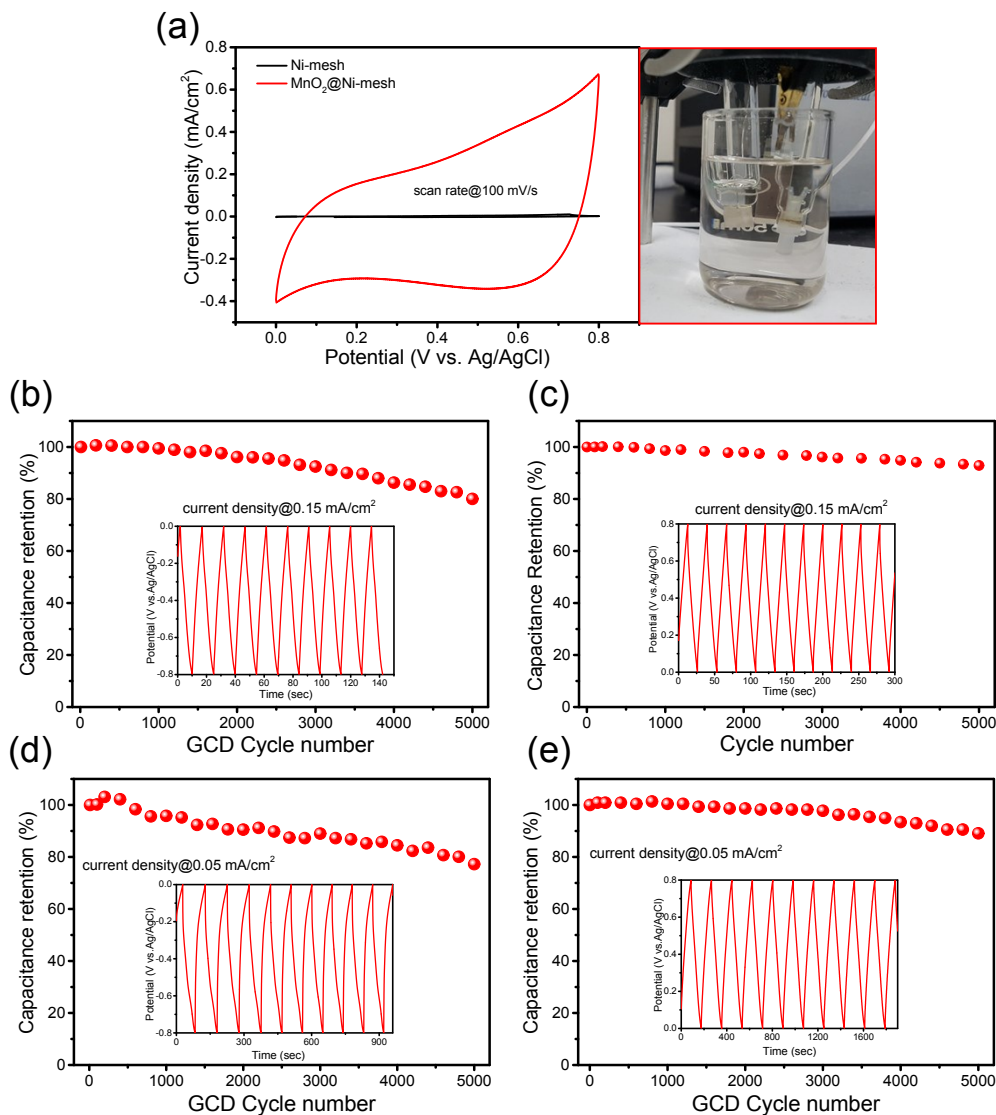
Fig. S8 Electrochemical measurements in a three-electrode configuration in 1 M Na_2SO_4 electrolyte: (a) CVs curve of the bare Ni-mesh in comparison with MnO_2@Ni-mesh network electrodes at the scan rate of 100 mV/s, suggesting a negligible contribution from Ni-mesh. Digital photograph of the electrode sample in CV running mode showing its high transparency (Right side). Long-term cycling stability performance: (b, c) MoS_2@Ni-mesh and MnO_2@Ni-mesh network electrodes, respectively measured at an applied current density of 0.15 mA/cm² (inset: 1st 10 cycles). (d, e) MoS_2@Ni-mesh and MnO_2@Ni-mesh network electrodes, respectively measured at an applied current density of 0.05 mA/cm² (inset: 1st 10 cycles).
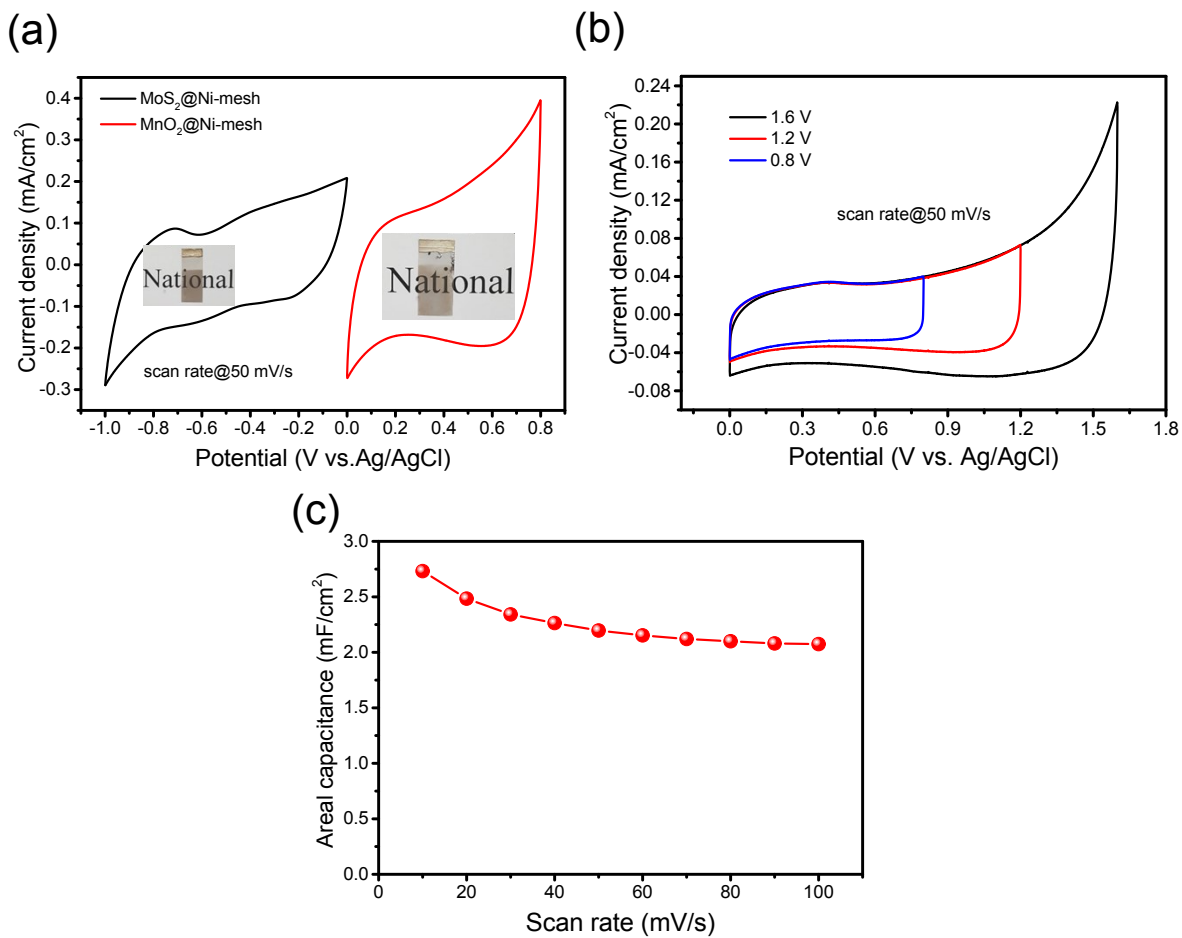
Fig. S9 (a) Comparison of CV curves for the MoS_2@Ni-mesh and MnO_2@Ni-mesh network electrode at 50 mV/s. (b) Characteristic CV curve at different potential windows. (c) The areal capacitance of the FT-ASSc device as a function of scan rate measured from the CV curve (Fig. 6b).
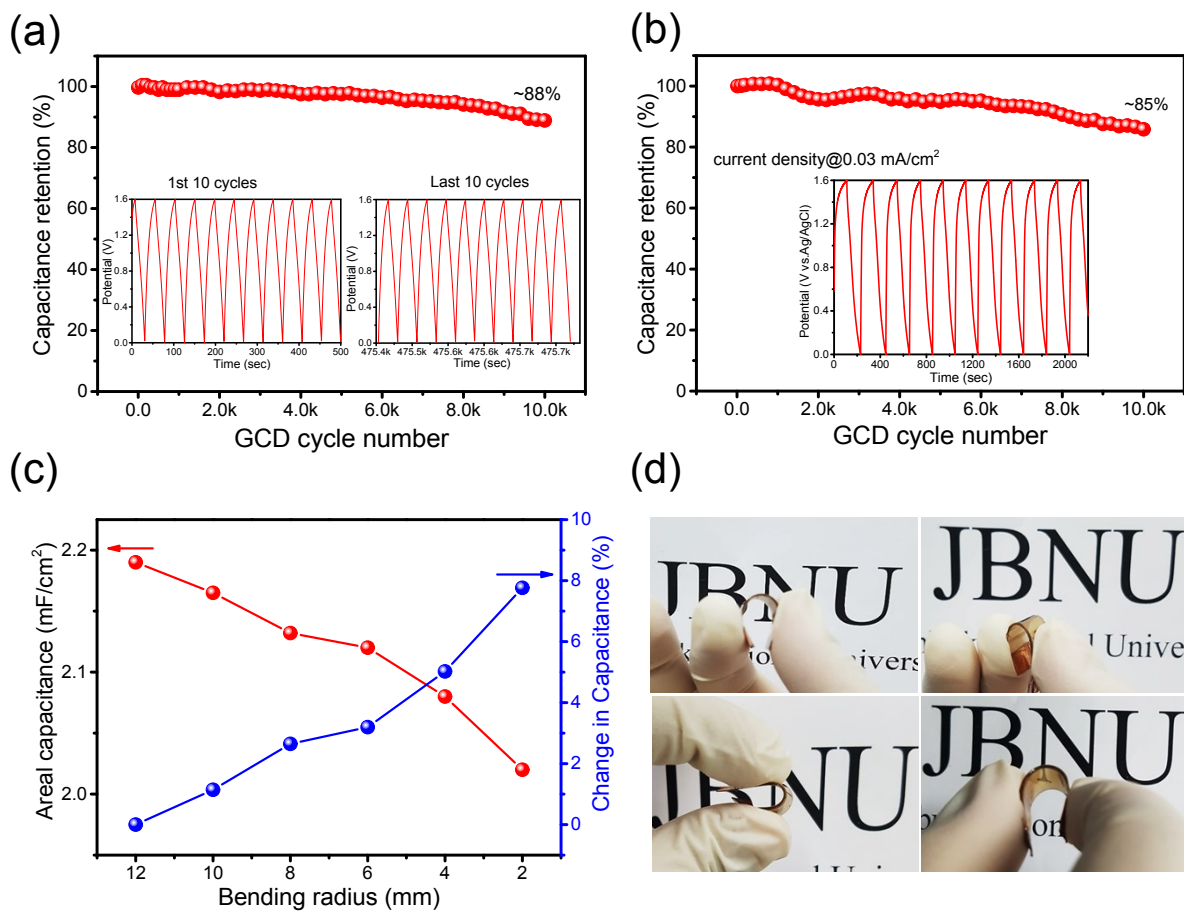
Fig. S10 Long-term cycling stability performance of the FT-ASSc device measured at an applied current density of (a) 0.08 mA/cm² (inset: 1st 10 cycles and last 10 cycles showing the high stability of the device), and (b) 0.03 mA/cm² (inset: 1st 10 cycles). (c) Change in areal capacitances (mF/cm²) and change in capacitance (%) as a function of bending radii. (d) Digital photographs of the FT-ASSc device bending at different bending conditions.
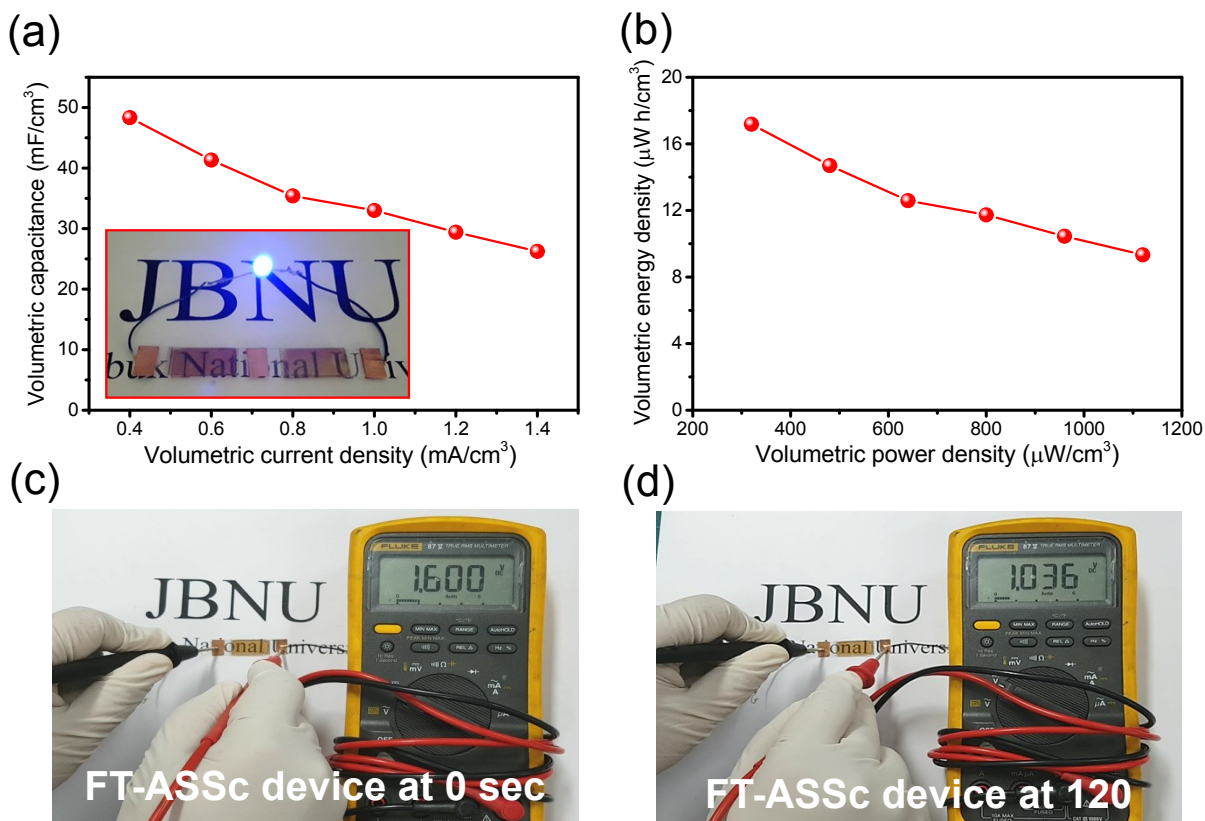
Fig. S11 (a) The volumetric capacitance of the FT-ASSc device as a function of volumetric current density (inset: illuminating a BLUE LED by two FT-ASSc devices connected in series). (b) Volumetric energy density vs power density plot of the FT-ASSc device. (c and d) Digital photograph of a fully charged FT-ASSc device voltage (V) measured by a multimeter at different times.
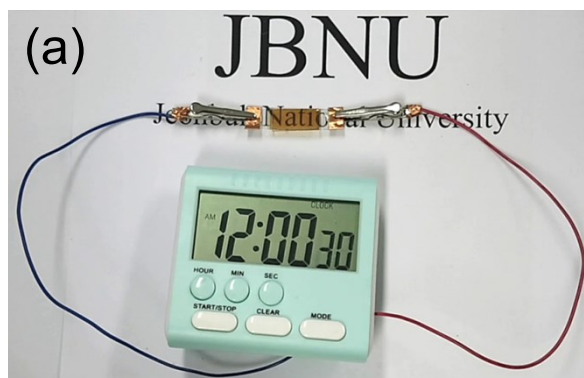
Fig. S12 Digital photographs of a digital clock power up by a single FT-ASSc device at a different time scale: (a) 30 sec (b) 1 min 30 sec and (c) 2 min 30 sec demonstrating the high energy density and power density of the FT-ASSc device.

Movie MVS1. A digital clock powered by a single FT-ASSc for 3 min (mp.4)

Fig. S13 Measurement of resistance during Repeated scotch tape test for (a) 1st cycle and (b) 10th cycles, and (c) 30th cycles

Table S1. Comparison of the areal capacitance, transparency, specific scan rates/GCD current densities, and potential window of various transparent supercapacitor devices with the present work.
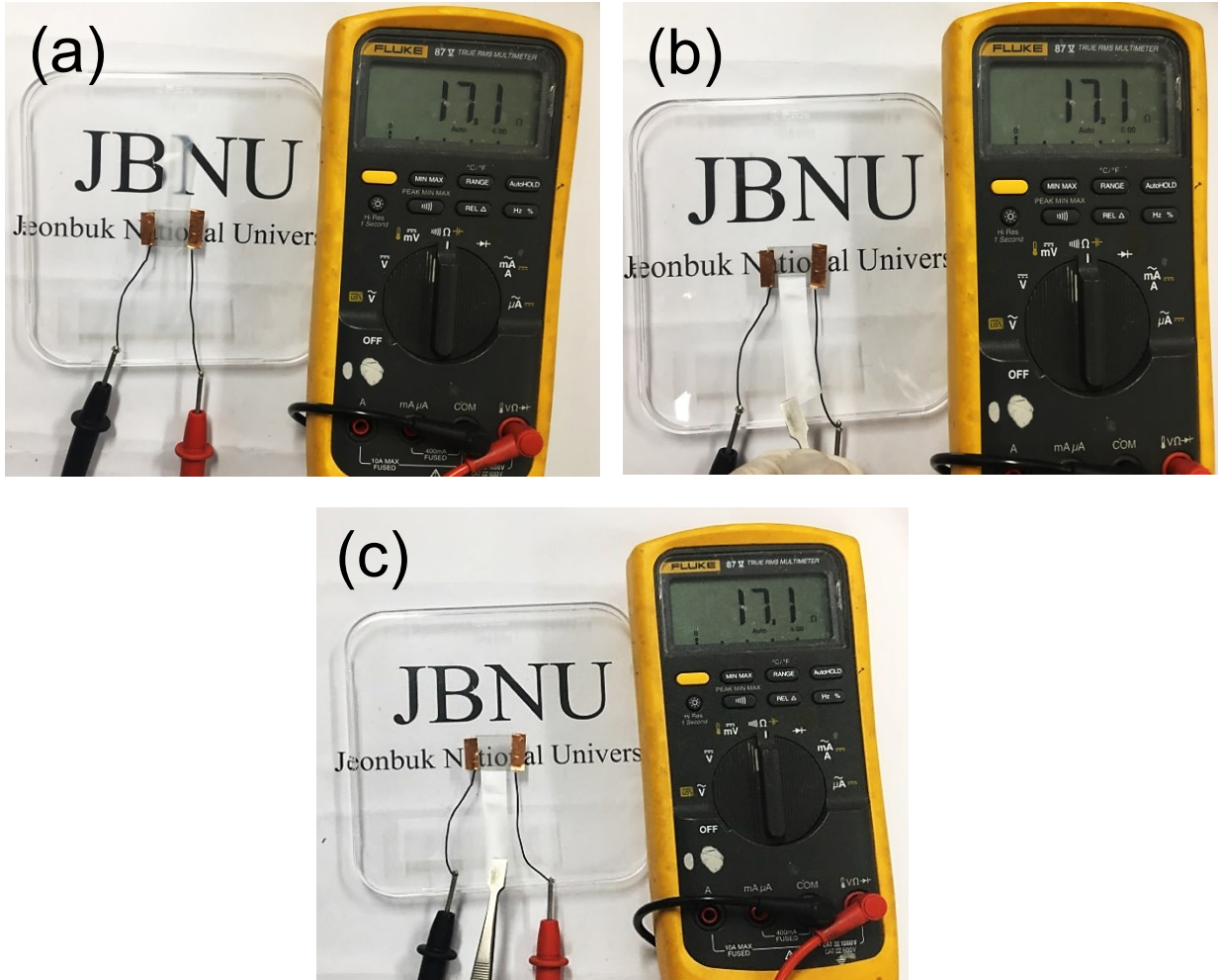
Material	C/A (mF/cm^2)	Scan rate (V/s)/current density (A/cm^2)	Transmittance (T%)	Potential window (V)	Reference
Au@MnO$_2$ supercapacitor	0.795	5 μA/cm^2	36	1.0 V	[1]
Graphene	3.3	0.02 mA/cm^2	47	1.0 V	[2]
GNHC-GF (Symmetric device)	5.48	0.015 mA/ cm^2	44	1.0 V	[3]
Ag/Au/PPy	0.58	5.8 μA/cm^2	64	0.8 V	[4]
RuO$_2$/PEDOT supercapacitor device (Symmetric device)	0.84	10 mV/s	80	0.8 V	[5]
RuO$_2$/PEDOT supercapacitor device (Asymmetric device)	1.06	50 mV/s	78	1.2 V	[5]
Ti$_3$C$_2$T$_x$ (Symmetric device)	0.87	2 μA/cm^2	80	0.6 V	[6]
Ti$_3$C$_2$T$_x$ (Asymmetric device)	1.4	4 μA/cm^2	72	1.0 V	[6]
PEDOT:PSS/AgNWs	0.6	50 mV/s	~51	0.8 V	[7]
ITO/Co$_3$O$_4$	6.03	1 mV/s	51	0.8 V	[8]
In$_2$O$_3$/SWCNT In sphere	0.81	20 mV/s	79	0.8 V	[9]
MnO$_2$/ITO/PET	4.73	50 μA/cm^2	44	0.8 V	[10]
ITO/Ni@Gr-TF/Fe@Gr-TF	10.9	20 mV/s	51	1.0 V	[11]
AgNW/rGO/PANI(Symmetric device)	6.4	0.08 mA/cm^2	57	1.0 V	[12]
Co(OH)$_2$/AgNWs (Symmetric device)	0.9	10 mV/s	~73	0.6 V	[13]
FT-ASSc device (Asymmetric device)	**2.73**	**10 mV/s**	**~50**	**1.6 V**	**This work**

Table S2. Comparison of the areal capacitance, specific scan rates/GCD current densities, transparency, potential window, the stability of various transparent supercapacitor electrodes with the present work.

Material	C/A (mF/cm^2)	Scan rate (V/s)/current density (A/cm²)	Transmittance (T%)	Potential window (V)	Stability Cycle	Reference
Au@MnO$_2$ supercapacitor	4.72	5 µA/cm²	~48	0.0-1.0	-	[1]
RuO$_2$/PEDOT	2.2	5 mV/s	~89	0.0-0.8	-	[5]
Ti$_3$C$_2$T$_x$	3.4	10 mV/s	~40	-0.15-0.5	-	[6]
Fe@Gr-TF	76.5	0.2 mA/cm²	~70	-1.25-0.0	1000 (~76% retention)	[11]
Co(OH)$_2$/AgNWs	5.18	10 mV/s	~73	0.0-0.6	-	[13]
PEDOT:PSS	1.18	0.025 mA/cm²	65	0.0-0.8	1000	[14]
Au/MnO$_2$ network	3.23	0.005 mA/cm²	~76	0.0-0.8	500	[15]
Embedded Ag Grid electrode	2.79	10 mV/s	~81	0.0-0.8	10,000 (~92% retention)	[16]
Embedded Ni mesh/PEDOT:PSS	0.52	50 mV/s	~83	0.0-0.8	5000 (~95% retention)	[17]
MnO$_2$@Ni	80.7	5 mV/s	~80		10,000 (~96% retention)	[18]
HTSE film	3.64	10 mV/s	~85	0.0-1.0	10,000 (~95% retention)	[19]
AgNWs/NiOH/PEDOT:PSS	3.45	10 mV/s	86	0.0-0.8	-	[20]
MnO$_2$@AuNFs	8.26	5 mV/s	86	0.0-0.8	10,000 (~94% retention)	[21]
MoS$_2$@Ni-mesh (negatrode)	**7.31**	**10 mV/s**	**~70**	**-1.0-0.0**	**5000 (~80% retention)**	**This work**
MnO$_2$@Ni-mesh (positrode)	**9.73**	**10 mV/s**	**~75**	**0.0-0.8**	**5000 (~90% retention)**	**This work**

Table S3. Power densities, energy densities, potential window, and stability of our FT-ASSc device in comparison with the reported transparent supercapacitor devices.

Active material	Power density ($\mu W/cm^2$)	Energy density ($\mu Wh/cm^2$)	Potential Window (V)	Transmittance (T%)	Stability Cycle	Ref
$Ti_3C_2T_x$ (Asymmetric)	2.36	0.049	1.0 V	72%	20,000 (~100% capacitance retention)	[6]
	4.33	0.034				
	8.29	0.025				
	16.44	0.02				
	25.37	0.018				
Ruo_2/PEDOT:PSS	0.28	0.015	0.8 V	~80%	10,000 (~84% capacitance retention)	[5]
	1.13	0.014				
	2.08	0.014				
	4.83	0.014				
	19.47	0.011				
Ag NW/Ni(OH)$_2$-PEIE/PEDOT:PSS	3.2	0.074	0.8 V	~80%	10,000 (~92% capacitance retention)	[20]
	4	0.072				
	6	0.069				
	12	0.059				
	20	0.05				
MnO_2@AuNFs	4	0.143	0.8 V	~79%	10,000 (~95% capacitance retention)	[21]
	8	0.101				
	12	0.078				
	16	0.066				
	20	0.054				
Co(OH)$_2$/AgNWs	28.8	0.04	0.6 V	~54%	10,000 (~91% capacitance retention)	[13]
	43.5	0.0375				
	57.3	0.035				
	70.6	0.0335				
	83.1	0.03				
NiCoS@Ni@Cu NFs	11.16	0.49	0.8 V	~65%	10,000 (~90% capacitance retention)	[22]
	15.27	0.34				
	19.18	0.27				
	22.82	0.21				
	26.18	0.17				
MoS_2@Ni-mesh/MnO_2@Ni-mesh (FT-ASSc device)	**16**	**0.86**	**1.6 V**	**~50%**	**10,000 (~88% capacitance retention)**	**This work**
	24	**0.73**				
	32	**0.63**				
	40	**0.59**				
	42	**0.52**				

Reference

[1]   T. Qiu, B. Luo, M. Giersig, E.M. Akinoglu, L. Hao, X. Wang, L. Shi, M. Jin, L. Zhi, *Small*, 2014, **10**, 4136–4141.

[2]   N. Li, G. Yang, Y. Sun, H. Song, H. Cui, G. Yang, C. Wang, *Nano Lett.*, 2015, **15**, 3195–3203.

[3]   N. Li, X. Huang, H. Zhang, Z. Shi, C. Wang, *J. Mater. Chem. A*, 2017, **5**, 16803.

[4]   H. Moon, H. Lee, J. Kwon, Y.D. Suh, D.K. Kim, I. Ha, J. Yeo, S. Hong, S.H. Ko, *Sci. Rep.*, 2017, **7**, 41981.

[5]   C. (John) Zhang, T.M. Higgins, S.H. Park, S.E. O'Brien, D. Long, J.N. Coleman, V. Nicolosi, *Nano Energy*, 2016, **28**, 495–505.

[6]   C.J. Zhang, B. Anasori, A. Seral-Ascaso, S.H. Park, N. McEvoy, A. Shmeliov, G.S. Duesberg, J.N. Coleman, Y. Gogotsi, V. Nicolosi, *Adv. Mater.*, 2017, **29**, 1–9. doi:10.1002/adma.201702678.

[7]   X. Liu, D. Li, X. Chen, W.Y. Lai, W. Huang, *ACS Appl. Mater. Interfaces,* 2018, **10**, 32536–32542.

[8]   X.Y. Liu, Y.Q. Gao, G.W. Yang, *Nanoscale,* 2016, **8**, 4227–4235.

[9]   P. Chen, G. Shen, *Appl. Phys. Lett.*, 2009, **94**, 043113 1.

[10]   Y. Wang, W. Zhou, Q. Kang, J. Chen, Y. Li, X. Feng, D. Wang, Y. Ma, W. Huang, *ACS Appl. Mater. Interfaces,* 2018, **10**, 27001–27008.

[11]   N. Li, X. Huang, H. Zhang, *J. Alloy. Compounds*, 2017, **712**, 194.

[12]   F. Chen, P. Wan, H. Xu, X. Sun, *ACS Appl. Mater. Interfaces*, 2017, **9**, 17865–17871.

[13]   H. Sheng, X. Zhang, Y. Ma, P. Wang, J. Zhou, Q. Su, W. Lan, E. Xie, and C. John Zhang, , *ACS Appl. Mater. Interfaces*, 2019, **11**, 8992–9001.

[14]   T. Cheng, Y. Z. Zhang, J. D. Zhang, W.Y. Lai, W. Huang, *J. Mater. Chem. A,* 2016, **4**, 10493–10499.

[15]   S. Kiruthika, C. Sow, G.U. Kulkarni, *Small,* 2017, **13**, 1–9.

[16]   J.L. Xu, Y.H. Liu, X. Gao, Y. Sun, S. Shen, X. Cai, L. Chen, S.D. Wang, *ACS Appl. Mater. Interfaces,* 2017, **9**, 27649–27656.

[17]   Y.H. Liu, J.L. Xu, S. Shen, X.L. Cai, L. Sen Chen, S.D. Wang, *J. Mater. Chem. A,* 2017, **5**, 9032–9041.

[18]   Y.H. Liu, J.L. Xu, X. Gao, Y.L. Sun, J.J. Lv, S. Shen, L. Sen Chen, S.D. Wang, *Energy Environ. Sci.*, 2017, **10**, 2534.

[19]   S. B. Singh, T. Kshetri, Th. I. Singh, N. H. Kim, J. H. Lee, *Chemical Engineering Journal*, 2019, 359, 197.

[20]   R.T. Ginting, M.M. Ovhal, J.W. Kang, *Nano Energy*, 2018, **53,** 650–657.

[21]   S. B. Singh, T. I. Singh, N. H. Kim, J. H. Lee, *J. Mater. Chem. A*, 2019, **7**, 10672–10683.

[22]   S. B. Singh, T. I. Singh, J. Dai, T. Kshetri, N.H. Kim, J. H. Lee, *Chemical Engineering Journal*, 2020, **395**, 125019 oi.org/10.1016/j.cej.2020.125019